(Received 28 June 2024, Accepted 12 August 2024, Scheduled 30 August 2024)

Design and Optimization of Integrated Symmetrical Coil Structure for Dynamic Wireless Power Transmission System for Autonomous Rail Rapid Transit

Yu Cheng[1], Wei Shi[1,*], Zhongqi Li[1,2,3], Jianbin Wang[1], and Zhenhui Wu[1]

[1] College of Railway Transportation, Hunan University of Technology, Zhuzhou 412007, China
[2] College of Electrical and Information Engineering, Hunan University, Changsha 412008, China
[3] College of Electrical and Information Engineering, Hunan University of Technology, Zhuzhou 412007, China

ABSTRACT: In this paper, to address the low transmission efficiency problem caused by large magnetic leakage and insufficient anti-deviation performance, an integrated symmetrical coil (ISC) structure is proposed. The ISC structure eliminates the need for an external active shielding coil to counteract the leaked magnetic field, and enhances anti-offset performance by utilizing an integrated coil. Additionally, a deep learning-based method for optimizing the coil structure is employed to determine the optimal parameters. The theoretical simulation is validated using Maxwell software, and based on this, the design and parameters of the ferrite structure are adjusted to improve the magnetic shielding effect and transmission efficiency of the coil. Subsequently, a 2 kW prototype experiment is conducted to validate the findings. Results indicate that when the ISC structure is offset by 200 mm in the X-direction, the research demonstrates that the coupling coefficient fluctuation remains below 5%, achieving a transmission efficiency of up to 96.37%. Furthermore, the magnetic leakage is significantly reduced to below 27 μT at 800 mm on both sides of the door in the X-direction.

1. INTRODUCTION

Rail transportation is currently one of the most important modes of transportation in China, connecting various regions. In the country, transportation modes include electric buses, smart rail, light rail, and subway systems [1–3]. In recent years, electric vehicles have been strongly promoted by the government due to their adaptability, lack of pollution, and other advantages, and people have begun to pay widespread attention to wireless power transmission (WPT) technology [4, 5]. WPT technology generates voltage to power electric vehicles through a magnetic field transformed in space, which is different from traditional energy transmission through wires. Moreover, WPT technology effectively solves the problems of poor environmental adaptability, easy spark production, and other safety hazards associated with traditional charging methods. Therefore, WPT technology holds promising market prospects in the electric vehicle market [6, 7].

When WPT technology is applied to electric vehicles, the design of the coupling mechanism becomes critical [8]. If there is an offset between the transmitting coil and the receiving coil, the coupling coefficient between the two coils will fluctuate, affecting the energy transfer efficiency of the system. In addition, when wireless charging is performed in an electric vehicle, strong leakage fields are generated around the vehicle. This leakage field will increase with the charging level, affecting not only the surrounding electronic devices but also human health [9, 10]. Therefore, it is especially important to study the anti-offset and magnetic shielding technology of the coil structure of WPT system. This will undoubtedly become one of the key development directions of WPT technology in the future [11].

Since 1988, when Boys team at the University of Auckland started studying inductively coupled wireless energy transmission technology, various magnetic coupling structures have been designed in the field of coil offset resistance [12], in which a method was proposed to enhance the coil offset resistance by changing the details of the DD (Double-D) Coil aspect ratio, coil coverage area, and overlap ratio, but it was also accompanied by the issue of low transmission efficiency. In [13], the team proposed a method to enhance the transmission efficiency and offset distance of the coil through overlapping. Although the offset distance and transmission efficiency can reach 170 mm and 95%, it does not consider the significant magnetic leakage problem of the WPT system.

In terms of magnetic shielding, it can be divided into two ways: active shielding and passive shielding. Passive shielding is a technology that weakens or eliminates the leaking magnetic field by using the original magnetic field in the WPT system. This is achieved through a designed shielding coil that induces a reverse canceling magnetic field without increasing the excitation source. In [14], the team from Southwest Jiaotong University, based on the single measurement point model proposed by Park and other scholars [15], extended the single point to a two-dimensional plane by establishing a new physical model. They calculated the optimal inductance using a functional rela-

* Corresponding author: Wei Shi (shiwei@hut.edu.cn).

tionship. However, this method is not applicable to the three-dimensional plane, which limits its practical value.

Active shielding is a technology that utilizes a weakening coil with an excitation source to generate a counteracting magnetic field in the opposite direction of the magnetic field of the coil in the WPT system, thus weakening or eliminating the magnetic field leaking out from the original coil. In [16], Cruciani and other Italian scholars proposed a method to suppress the magnetic field in a specific region of the space by placing the shielding coil in series with the transmitting coil on the same level. However, this method can only achieve the effect of weakening part of the leaked magnetic field, while ignoring the leakage of the WPT system as a whole.

An omnidirectional wrap-around active magnetic shielding structure is proposed in [17]. It effectively reduces the magnetic leakage problem on the target plane of the WPT system and possesses high transmission efficiency. However, the anti-offset performance of this proposed structure is poor. The inadequate offset resistance is a significant drawback of this structure.

Summarizing the above, it can be found that the currently proposed structure methods are in a single field, and there are few precedents of combining anti-offset technology with magnetic shielding technology. The purpose of this paper is to propose ideas and methods that can serve as a reference for the application of WPT technology in the field of rail transportation. For this purpose, this paper designs an integrated symmetric coil structure model and combines deep learning to propose a "solution-optimized" coil structure optimization process method. Simultaneously, it utilizes Maxwell software for system modeling and ferrite optimization, ultimately achieving significant progress. Building upon these outcomes, a 2 kW experimental model is constructed, demonstrating that the coupling coefficient's fluctuation rate remains below 5% even when the train's motion direction reaches a 200 mm offset. Moreover, the magnetic leakage at 800 mm on both sides of the door in the train's direction is significantly lower than 27 μT, and the transmission efficiency can reach up to 96.37% at the output.

2. COIL STRUCTURE AND PRINCIPLE

2.1. ISC Structure Design

From the current application of WPT in the field of Autonomous Rail Rapid Transit, the proposed new coil structure still sacrifices mutual inductance to reduce the coupling coefficient in exchange for stable transmission efficiency and does not take into account the hazards of magnetic leakage phenomenon on the equipment as well as the human body. In order to solve these problems, an ISC coil structure is proposed in this paper, as shown in Fig. 1, which not only enables the WPT system to have a large coupling coefficient even after the X-direction offset but also greatly reduces the leakage magnetic field at 800 mm on both sides of the door of the electric vehicle during the X-direction offset.

In this structure, the receiving coil R_x is composed of four square coils: R_{x1}, R_{x2}, R_{x3}, and R_{x4} of the same size. Among

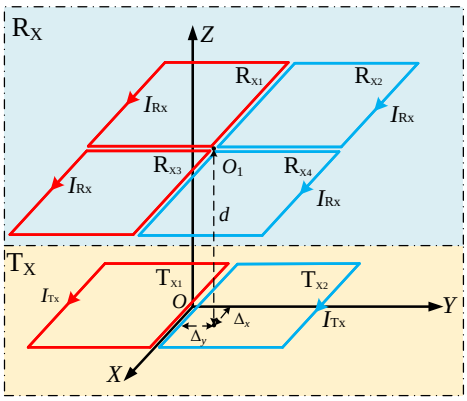

FIGURE 1. Schematic diagram of the ISC structure.

them, the currents in R_{x1} and R_{x3} flow in the same direction, but in the opposite direction to the currents in R_{x2} and R_{x4}. As shown in Figs. 2(a) and (b), the transmitting coil T_x comprises 2 square coils, T_{x1} and T_{x2}, identical to the R_{x1} and R_{x2} coils connected in series.

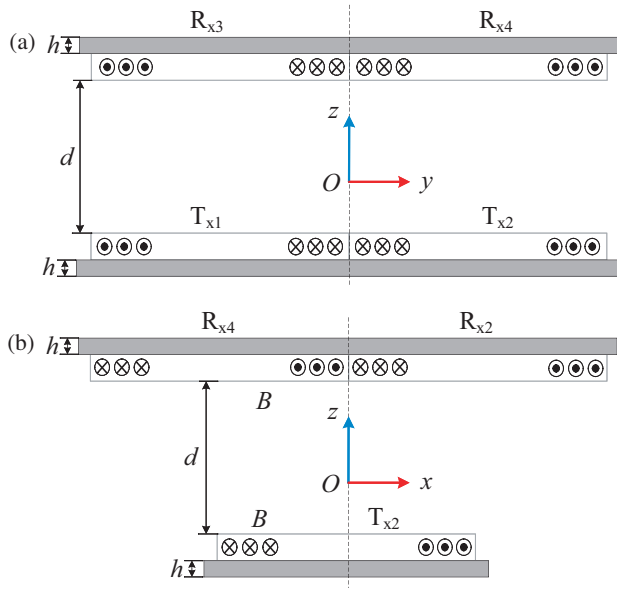

FIGURE 2. Side view of ISC structure in X- and Y-direction. (a) X direction. (b) Y direction.

2.2. Analysis of the Principle of Anti-Offset for ISC Structure

In order to analyze and demonstrate the anti-offset performance of the ISC structure, a simulation model of the ISC coil has been developed in this paragraph using the finite element software Ansys Maxwell. Since the ISC coil is a symmetrical structure, it can be divided into left and right parts when the anti-offset principle is analyzed, as illustrated in Fig. 3. In Fig. 3(a), when the transmitting coil T_x is directly opposite to the receiving coil R_x, the upward magnetic flux generated by the transmitting coil T_{x1} uniformly passes through the two receiving coils R_{x1} and R_{x3}. As the transmitting coil T_{x1} offsets in the X-direction, it moves away from R_{x1}, causing a decrease in the generated upward magnetic flux passing through R_{x1}, while getting closer to R_{x3}, resulting in an increase in flux passing through R_{x3}. Ul-

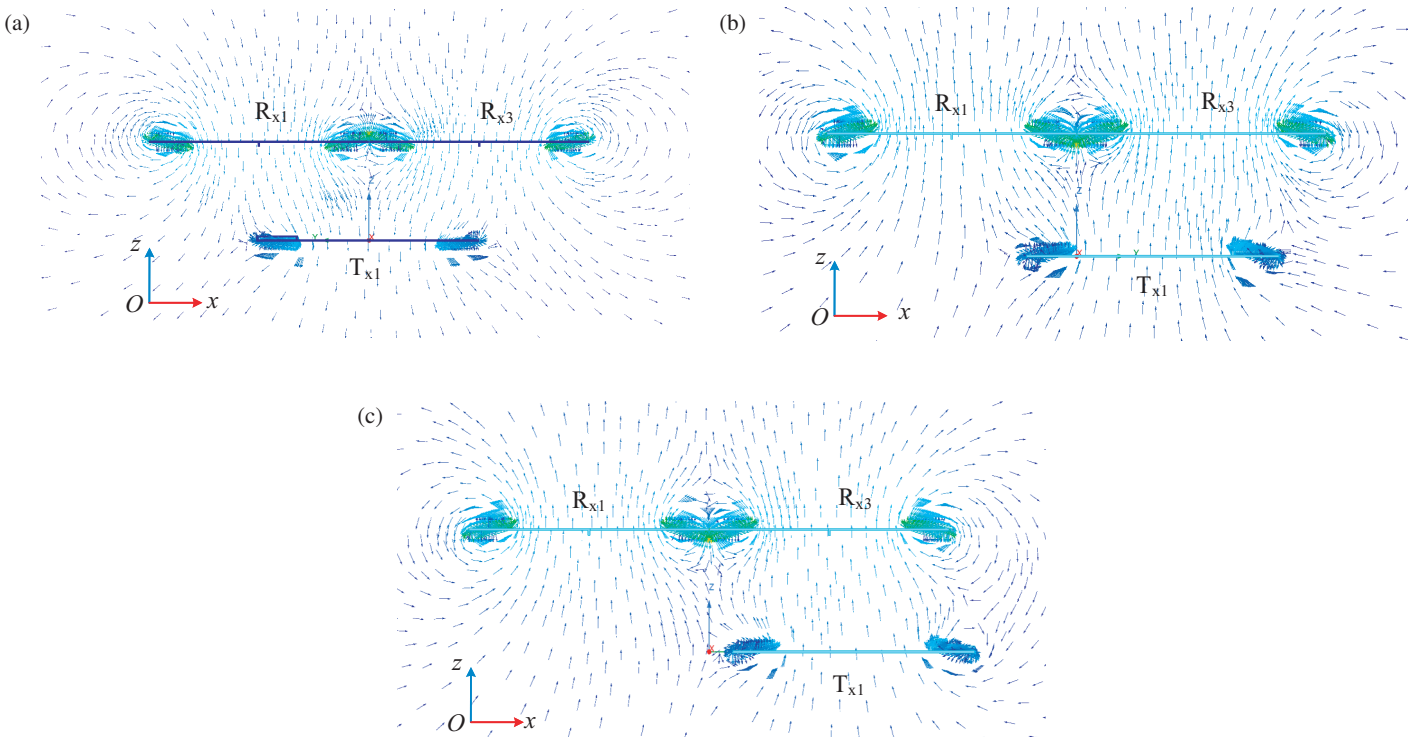

FIGURE 3. Simulation of the magnetic field distribution of the ISC structure offset along the X-direction. (a) Coil alignment ($\Delta X = 0$ mm). (b) X-direction offset ($\Delta X = 120$ mm). (c) X-direction offset ($\Delta X = 200$ mm).

timately, the magnetic flux passing between the coils is maintained at a constant state, enabling the coupling coefficient of the system to reach a quasi-constant state. In Fig. 3(b), when the transmitting coil T_{x1} is offset by 120 mm, the magnetic flux is most intense in the area adjacent to the edges of R_{x1} and R_{x3}, leading to the overall magnetic flux of the system reaching its maximum and the coupling coefficient being at its peak. In Fig. 3(c), as the transmitting coil offsets from 120 mm to 200 mm, the coupling coefficient between the coils decreases due to the decrease in longitudinal flux generated by the transmitting coil T_{x1} passing through the main coils R_{x1} and R_{x3} with the increase in offset distance. A similar principle applies between the individual transmitting coil T_{x2} and receiving coils R_{x2} and R_{x4}. Although there are up and down fluctuations in the coupling coefficients during the offset process, the coupling coefficients of the system as a whole can be maintained in a quasi-constant state.

2.3. Analysis of the Magnetic Shielding Principle of ISC Structure

Within the real-life field of rail transport, the width of relatively small-sized electric vehicles is generally 1600 mm. Therefore, the magnetic leakage observation plane set up in this paper is 800 mm from the midpoint of the receiving coil (β-plane at $+800$ mm and α-plane at -800 mm). As shown in Fig. 4, when the transmitting coil T_x moves in the X-direction, a top-down magnetic field is generated because the direction of the currents flowing in R_{x1} and R_{x3} is clockwise, whereas the currents flowing in R_{x2} and R_{x4} are anticlockwise, so a bottom-up magnetic field is generated. The specific weakening principle

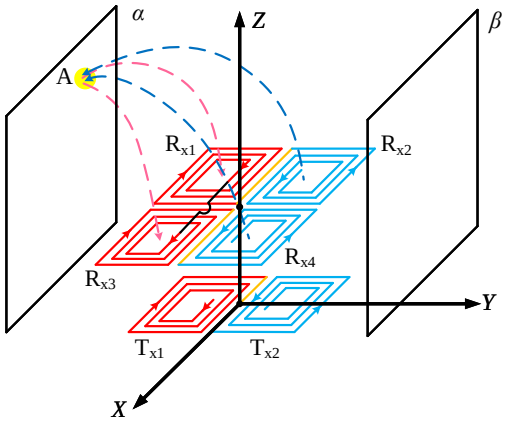

FIGURE 4. Schematic of the ISC structure at point A in the direction of the magnetic field.

is shown in Fig. 5. When the magnetic fields generated by the four receiving coils intersect with each other at point A on the α-plane at 800 mm, they will partially cancel each other, which achieves the purpose of weakening the leakage magnetic field.

In Fig. 5(a), B_{Rx1} represents the magnetic field produced by the receiving coil R_{x1}; B_{Rx2} represents the magnetic field produced by the receiving coil R_{x2}; B_{Rx3} represents the magnetic field produced by the receiving coil R_{x3}; and B_{Rx4} represents the magnetic field produced by the receiving coil R_{x4}. B_{Rx1} is decomposed into B_{Rx1-X} and B_{Rx1-Y} in the X and Y directions; B_{Rx2} is decomposed into B_{Rx2-X} and B_{Rx2-Y} in the X and Y directions; B_{Rx3} is decomposed into B_{Rx3-X} and B_{Rx3-Y} in the X and Y directions; and B_{Rx4} is decom-

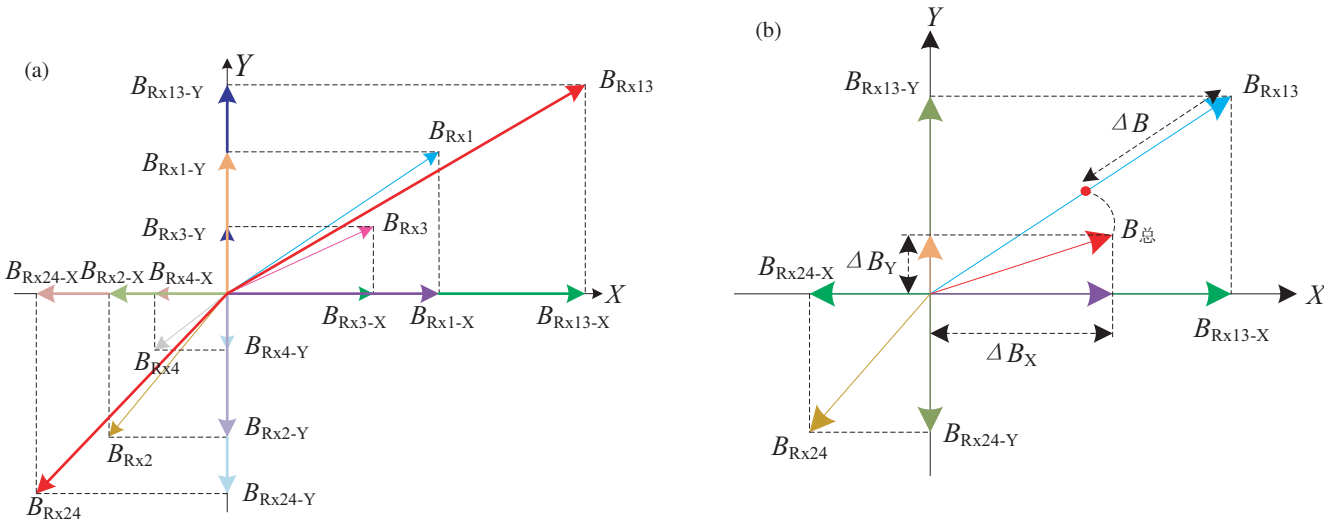

FIGURE 5. Vector analysis diagram of electromagnetic shielding for ISC structure.

posed into B_{Rx4-X} and B_{Rx4-Y} in the X and Y directions. As the magnetic fields generated by coils R_{x1} and R_{x3} are in the same direction, vector synthesis is performed to generate B_{Rx13}. Similarly, coils R_{x2} and R_{x4} produce identical magnetic fields, so vector synthesis is carried out to generate B_{Rx24}.

In Fig. 5(b), B_{Rx13} represents the total magnetic field produced by coils R_{x1} and R_{x3} at point A in the α-plane. B_{Rx13} is further divided into B_{Rx13-X} and B_{Rx13-Y} in the X and Y directions. Similarly, B_{Rx24} denotes the total magnetic field generated by coils R_{x2} and R_{x4} at point A in the α-plane, which can be separated into B_{Rx24-X} and B_{Rx24-Y} in the X and Y directions. As B_{Rx13} and B_{Rx24} act in opposite directions, their X and Y components are combined and subtracted algebraically to synthesize the final total magnetic field, where ΔB represents the amount of leakage magnetism intercepted. This electromagnetic shielding effect is consistent across all points in the α and β planes, providing magnetic shielding capabilities throughout the plane to reduce the impact of leakage magnetic fields.

3. OPTIMISATION OF ISC STRUCTURE

3.1. Coupling Coefficients and Magnetic Field Calculation Methods for Coil Structures

To enhance the optimization of the ISC coil structure parameters, this section presents a method for calculating the magnetic induction strength of rectangular coils using vector magnetic potentials. Additionally, a quick method for determining the coupling coefficients of rectangular coils, as discussed in the [18], is introduced. Fig. 6 illustrates a schematic representation of the spatial arrangement of two traditional rectangular coils, labeled as 1 and 2, positioned in a three-dimensional plane. The dimensions of coil 1 are represented by a_1 (half-length) and a_2 (half-width), while coil 2 is defined by b_1 (half-length) and b_2 (half-width). The distances between the origin point O and the centers of coils 1 and 2 are denoted by s_1 and s_2, respectively. The target plane α is situated at a fixed distance of

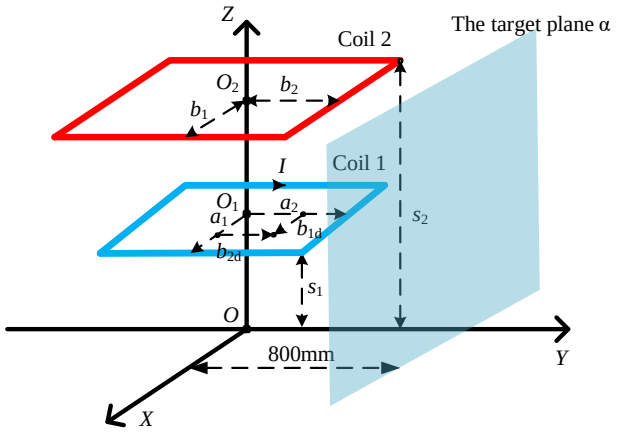

FIGURE 6. Schematic diagram of two rectangular coils.

800 mm from the centers of coils O_1 and O_2. The parameter I represents the current passing through coil 1.

Set any arbitrary point Q (x, y, z) in space in Fig. 6 with the following vector magnetic potential expression:

$$A(x,y,z) = \frac{\mu_0}{4\pi}\int_v \frac{J(x',y',z')\,dv'}{Dr} \tag{1}$$

where $\mu_0 = 4\pi * 10^{-7}$ is the magnetic permeability in air; J represents the current density; v denotes the current distribution within the conductor; and D_r is the distance from any point Q to the point source (x', y', z'). It is known that the incident magnetic flux density is related to the magnetic vector position by the following equation:

$$B_0 = \nabla \times A \tag{2}$$

Magnetic flux density B_i under the expression of X-axis, Y-axis, and Z-axis:

$$B_{ix} = \frac{1}{4\pi^2}\int_{-\infty}^{\infty}\int_{-\infty}^{\infty} C_{ix}e^{-kz}e^{j(x\xi+y\eta)}d\xi d\eta \tag{3}$$

$$B_{iy} = \frac{1}{4\pi^2}\int_{-\infty}^{\infty}\int_{-\infty}^{\infty} C_{iy}e^{-kz}e^{j(x\xi+y\eta)}d\xi d\eta \quad (4)$$

$$B_{iz} = \frac{1}{4\pi^2}\int_{-\infty}^{\infty}\int_{-\infty}^{\infty} C_{iz}e^{-kz}e^{j(x\xi+y\eta)}d\xi d\eta \quad (5)$$

Style:

$$C_{ix} = \frac{-j2\mu_0 I\sin(\xi a_1)\sin(\eta a_2)}{\eta}\cdot e^{s_1 k} \quad (6)$$

$$C_{iy} = \frac{-j2\mu_0 I\sin(\xi a_1)\sin(\eta a_2)}{\xi}\cdot e^{s_1 k} \quad (7)$$

$$C_{iz} = \frac{-2\mu_0 Ik\sin(\xi a_1)\sin(\eta a_2)}{\xi\eta}\cdot e^{s_1 k} \quad (8)$$

ξ and η are the variables in the double Fourier integral variables:

$$q = \sqrt{\xi^2+\eta^2} \quad (9)$$

Therefore, the magnetic flux density can be expressed as:

$$B = |B| = \sqrt{|B_{\text{ix}}|^2 + |B_{\text{iy}}|^2 + |B_{\text{iz}}|^2} \quad (10)$$

In the practical application of dynamic wireless charging in Autonomous Rail Rapid Transit, the influence of the magnetic field leakage around the system on the human body and equipment needs to be taken into account. Therefore, in this paper, the magnetic leakage is reduced at a target surface 800 mm from the center of the automotive chassis, as shown in Fig. 6. Meanwhile, in general, the coupling coefficients between two conventional rectangular coils 1 and 2 at any position in three-dimensional space are expressed as follows:

$$k = \frac{M_{12}}{\sqrt{L_1 L_2}} \quad (11)$$

where M_{12} is the mutual inductance between coil 1 and coil 2. L_1 and L_2 are the self-inductances of coil 1 and coil 2, respectively. Therefore, before calculating the coupling coefficient of the proposed coil structure, its mutual inductance and self-inductance need to be calculated. In this paper, the expression for the mutual inductance between coil 1 and coil 2 is quoted as follows based on [18]:

$$M_{ab} = \frac{1}{4\pi^2 I}\int_{-\infty}^{\infty}\int_{-\infty}^{\infty}(C_{iz}+C_{ix})\frac{e^{j(b_{1d}+b_1)\xi} - e^{j(b_{1d}-b_1)\xi}}{j\xi} \cdot\frac{e^{j(b_{2d}+b_2)\eta} - e^{j(b_{2d}-b_2)\eta}}{j\eta}e^{-ks_2}\,d\xi d\eta \quad (12)$$

Using the above method, the calculation of mutual inductance between multiple coils can be summarized by the following equation:

$$M = \sum_{m=1}^{N_1}\sum_{n=1}^{N_2} M_{mn} \quad (13)$$

Here, N_1 and N_2 represent the number of turns for coils 1 and 2, respectively, with m denoting the turn index of coil 1 and n representing the turn index of coil 2. In the same way, the following self-inductance formula can be obtained:

$$L = \frac{1}{I}\iint_D B_z\,ds = \frac{1}{4\pi^2}\int_{-\infty}^{\infty}\int_{-\infty}^{\infty}\int_{-a_1}^{a_1}\int_{-a_2}^{a_2}\frac{-2\mu_0 q\sin(\xi a_1)\sin(\eta a_2)}{\xi\eta} \cdot e^{j(x\xi+y\eta)}\,dy\,dx\,d\xi\,d\eta \quad (14)$$

Based on Eqs. (13) and (14) and combined with the Newman formula, the following expressions for the self- and mutual inductances of the ISC coil can be obtained:

$$\begin{aligned} L_{\text{Tx}} =& L_{\text{Tx1}} + L_{\text{Tx2}} + 2M_{\text{Tx1-Tx2}} \\ L_{\text{Rx}} =& L_{\text{Rx1}} + L_{\text{Rx2}} + L_{\text{Rx3}} + L_{\text{Rx4}} + 2M_{\text{Rx1-Rx2}} \\ &+ 2M_{\text{Rx1-Rx3}} + 2M_{\text{Rx1-Rx4}} + 2M_{\text{Rx2-Rx3}} \\ &+ 2M_{\text{Rx2-Rx4}} + 2M_{\text{Rx3-Rx4}} \\ M_{\text{Tx-Rx}} =& M_{\text{Tx1-Rx1}} + M_{\text{Tx1-Rx2}} + M_{\text{Tx1-Rx3}} \\ &+ M_{\text{Tx1-Rx4}} + M_{\text{Tx2-Rx1}} + M_{\text{Tx2-Rx2}} \\ &+ M_{\text{Tx2-Rx3}} + M_{\text{Tx2-Rx4}} \end{aligned} \quad (15)$$

Finally, the coupling coefficient of the integrated coil can be quickly calculated according to Eq. (11).

By combining the above two methods, not only the coupling coefficient of the integrated coil can be calculated faster than that with the finite element simulation method, but also the magnetic field strength in the spatial α-plane can be calculated quickly. This establishes the theoretical foundation for the coil outcomes and the improvement of electromagnetic shielding effects in subsequent processes.

3.2. ISC Structural Parameter Optimisation Methods and Results

The relative position distribution between the transmitting and receiving coils, as well as their dimensional parameters, not only affect the stability of the coupling coefficient of the coil structure but also change the magnitude of the magnetic leakage of the whole WPT system. This ultimately leads to problems such as low overall transmission efficiency and a large magnetic leakage field of the WPT system. Therefore, this section focuses on the coupling coefficient k as the primary objective function. The magnetic field strength B on the α-plane at 800 mm on both sides of the door is used as the auxiliary constraint function. Through the formulas presented in this paper regarding the coupling coefficient and spatial electromagnetic field, the constraints are determined in conjunction with the actual requirements. Finally, a specific ISC solution optimization algorithm is employed to seek the optimal solution related to the primary objective function k. The parameter optimization of the ISC structure is carried out to achieve the goals of quasi-constant coupling coefficient and high transmission efficiency with low leakage.

3.2.1. Objective Function Set

In order to reduce the variable parameters, it is set that all the small coils forming the transmitting and receiving coils are square. Additionally, the relative transmission distance between the transmitting coil (T_x) and the receiving coil (R_x) is set to be 150 mm. The wire diameter (r) is 3.9 mm; the transmission power level (P) is 2 kW; the maximum fluctuation of the coupling coefficient (ε_X*) is 5%; and the safe leakage of the magnetic field as specified by the ICNIRP is $B = 27\,\mu$T. The fluctuation of the coupling coefficient (ε_X) is defined as follows:

$$\varepsilon_X = \left| \frac{k_{\Delta X} - k_0}{k_0} \right| \times 100\% \tag{16}$$

where k_0 denotes the coupling coefficient of the ISC when it is orthogonal, and $k_{\Delta X}$ denotes the coupling coefficient of the ISC when it is shifted in the X direction.

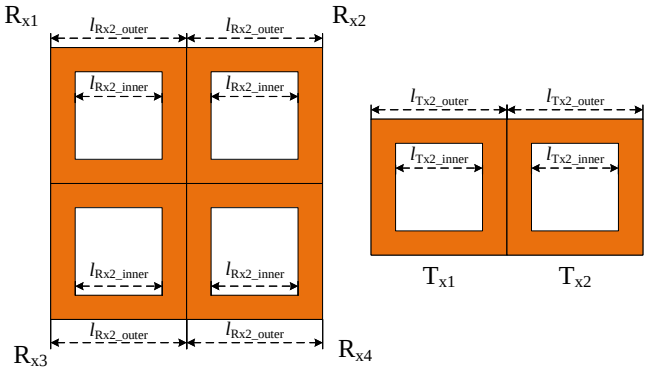

FIGURE 7. Top view of the ISC structure.

Therefore, coupling coefficient k is utilized as the primary objective function in the ISC solution optimization algorithm. The critical factors that can influence the coil k are also optimized, including the inner edge length $l_{\text{Tx1-inner}}$ of the transmitting coil, the inner edge length $l_{\text{Rx1-inner}}$ of the receiving coil (Fig. 7 shows the top view of the ISC coil structure), the number of turns N_{Tx} of the transmitting coil, and the number of turns N_{Rx} of the receiving coil. The first objective function concerning k is ultimately defined as:

$$\begin{aligned} \text{Fit} = k &= \frac{M}{\sqrt{L_1 L_2}} \\ &= f(l_{\text{Tx1-inner}}, l_{\text{Rx1-inner}}, N_{\text{Tx}}, N_{\text{Rx}}) \end{aligned} \tag{17}$$

where the mutual inductance M can be determined by Eq. (17). The self-inductances L_1 and L_2 can be found from Eqs. (15) and (16).

After determining the first objective function, the auxiliary constraint function related to the magnetic field strength B on the α-plane at 800 mm on both sides of the door is established. Given that the distance of the α-plane from the origin is fixed at 800 mm, it can be deduced from Eq. (10) that the current I_k is the sole factor influencing the magnetic field B when meeting the first objective function k. Consequently, the auxiliary constraint function is derived as:

$$\text{Fit} = B = f(I_{\text{k}}) \tag{18}$$

3.2.2. Setting of Constraint Conditions

Taking into account the length and width of the vehicles in the field of rail transport in real-life production, in order to find a more optimal solution for the ISC coil structure, a relatively wide but reasonable range of coil dimensions needs to be considered in the process of determining the optimal solution. Simultaneously, adhering to the safe magnetic leakage limit of $B = 27\,\mu$T specified by ICNIRP, the magnetic leakage of the designed coil structure must not exceed the specified value. Furthermore, to achieve the objectives of a quasi-constant coupling coefficient and high transmission efficiency, the set coupling coefficient fluctuation must be kept below the set $\varepsilon_{X*} = 5\%$, and the transmission efficiency must exceed 95%. Lastly, for safety considerations, the current flowing in the coil structure should be 20% lower than the current resistance of the selected wire diameter of 3.9 mm Leeds wire.

In summary, all the parameter constraint requirements are collated as follows:

$$\begin{cases} 170 \le l_{\text{Tx1 - inner}} \le 250 \\ 150 \le l_{\text{Rx1 - inner}} \le 230 \\ 10 \le N_{\text{Tx}} \le 20 \\ 10 \le N_{\text{Rx}} \le 20 \end{cases} \quad \begin{cases} \varepsilon_X{}^* \le 5\% \\ B \le 27 \\ 95\% \le \eta \\ I \le 80\% \cdot I_{\max} \end{cases} \tag{19}$$

3.2.3. Algorithm for the Optimal Solution

A flowchart of the ISC structure optimal solution algorithm is shown in Fig. 8. The detailed steps are as follows: firstly, the parameters $l_{\text{Tx1-inner}}$, $l_{\text{Rx1-inner}}$, N_{Tx}, and N_{Rx} to be optimized are binary coded, thus generating the initial category values and initial clusters associated with each parameter of the coil. Data processing is then performed to compute the desired coil objective function Fit=k and check to verify that the proposed constraints are not violated. After all constraints of the first objective function k are satisfied, the auxiliary constraint function B is further calculated and checked to verify that the auxiliary constraint function is satisfied. When all the constraints are satisfied, the judgment of the end condition is carried out, that is, whether the rate of change of the objective function is less than 10^{-6}. If it is satisfied, the objective function k is selected as the optimal individual, and the optimal solution is compiled to end the process, and if it is not satisfied, the genetic operation, i.e., interleaving, upgrading, and selecting, is carried out until the cut-off condition is satisfied. Finally, output the optimal parameters that satisfy the conditions, and the solutions for the optimal parameters are shown in Table 1.

3.3. Ferrite Optimisation and Simulation Results for ISC Structure

Ferrite is a metal oxide with ferromagnetic properties [19], characterized by low eddy current losses. Additionally, it pos-

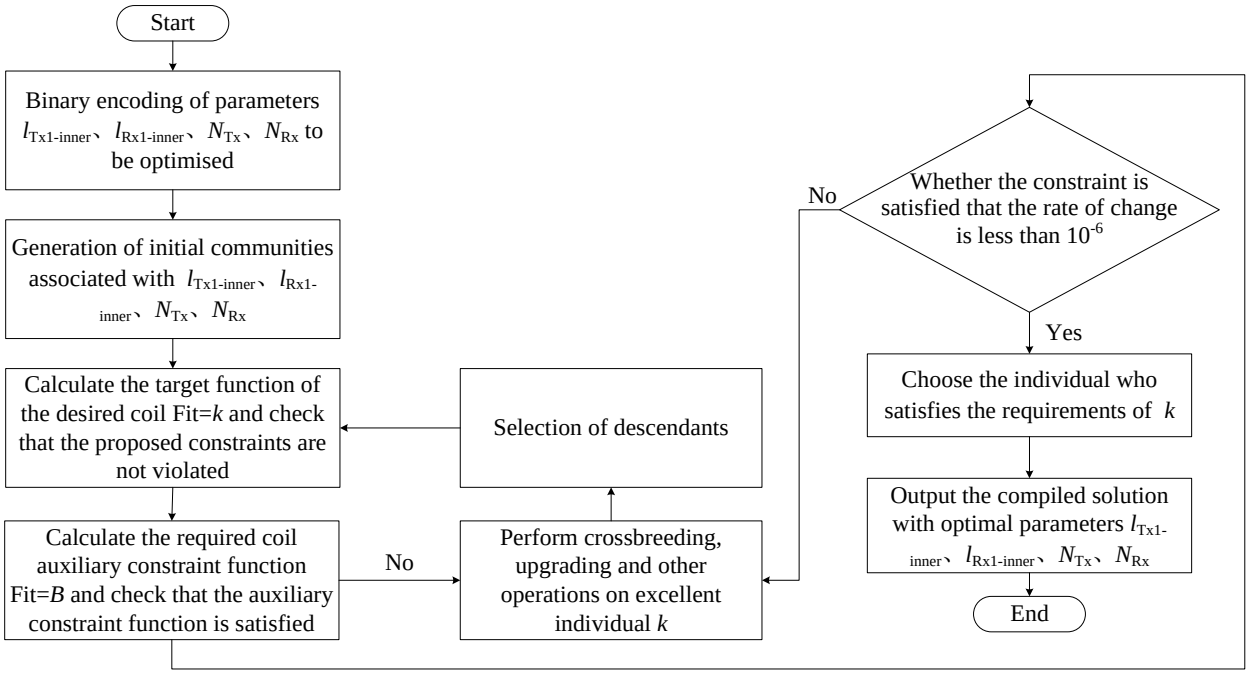

FIGURE 8. Flowchart of the optimal solution algorithm.

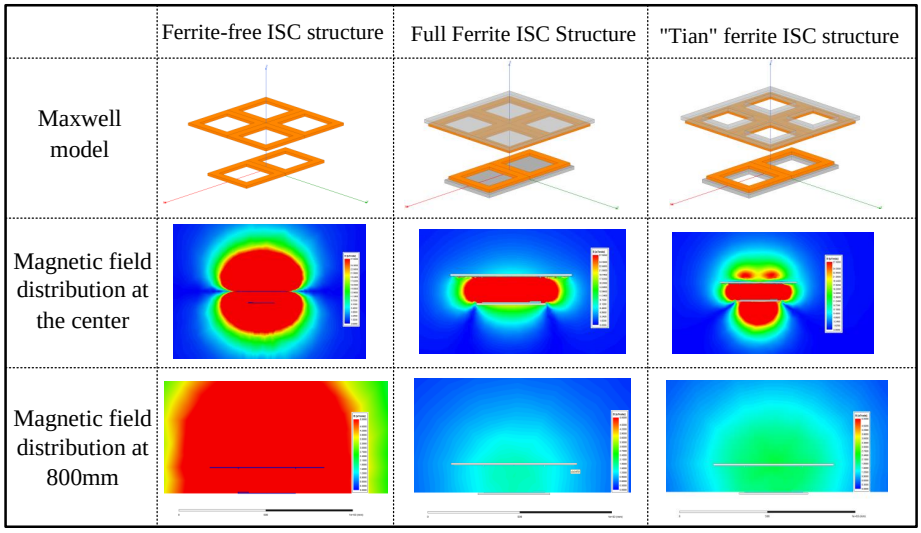

FIGURE 9. Leakage magnetic field diagrams of ISC structures under various ferrite shapes.

TABLE 1. Results of optimization of coupling coefficients for ISC structure.

Coils	Inner length/mm	Inner width/mm	Outer length/mm	Outer width/mm	Turns
T_{x1}	220	220	340	340	15
R_{x1}	220	220	340	340	15

sesses high resistivity and magnetic permeability, which reduces resistance to magnetic flux [20]. Consequently, ferrite can concentrate the magnetic field around the coil and guide the magnetic path, leading to an increase in the coupling coefficient of the coil. Moreover, ferrite is commonly used as a material for electromagnetic shielding [21]. In this paper, based on the optimization results of the coil parameters in Table 1, the coupling performance and electromagnetic shielding effect of coil structures with different ferrites were simulated by the Maxwell software. Fig. 9 shows the magnetic field distribu-

tion of various ferrite types. The figure demonstrates that compared to the ferrite-free ISC structure, the ISC structure with added "field" ferrite provides some magnetic shielding effect at 800 mm from both sides of the vehicle's driving direction and in the Z-direction, although there is still significant magnetic leakage in the Z-direction. Conversely, the addition of a ferrite block reduces magnetic leakage at 800 mm from both sides of the driving direction and in the Z-direction. Therefore, this paper optimizes a ferrite block with more detailed parameters.

Considering that the receiver coil is mounted underneath the chassis of the electric vehicle, its weight and size should be as small as possible to fit into the limited space. Therefore, it is dimensionally optimized by Maxwell software. Since the receiving coil of the ISC coil structure proposed in this paper is square, the considered ferrite is also designed to be square. The dimensions of the receiving coil ferrite are set to be $w_1 * w_1$, and the dimensions of the transmitting coil ferrite are set to be $w_1 * w_2$. In the analysis process, with reference to the national standard GB/T 38775 and the relevant requirements of SAE under high power, the ferrite thickness $h = 10$ mm is selected. In addition, combining the optimization results of the coil parameters in Table 1, the actual production and the material dimensions of the laboratory equipment, the size of the transmitting coil ferrite width w_2 is set to 400 mm, while the range of w_1 is set to 650 mm–750 mm. Finally, finite element simulation is carried out using Maxwell software. The results are shown in Fig. 10, and it can be found that the coupling coefficient k between the transmitting and receiving coils in the figure shows a decreasing trend in general with the increase of w_1, but the change is not large. Meanwhile, the fluctuation rate of the coupling coefficient of the coil after 200 mm offset from the orthogonal time shows drastic up and down fluctuations. It can be found that the fluctuation rate of the coupling coefficient during the offset process is the smallest at $w_1 = 700$ mm, which is 4.53%. Finally, considering the size of the ferrite, consumables, magnetic field, transmission stability, and other factors, the final size of the ferrite selected in this paper is shown in Fig. 11.

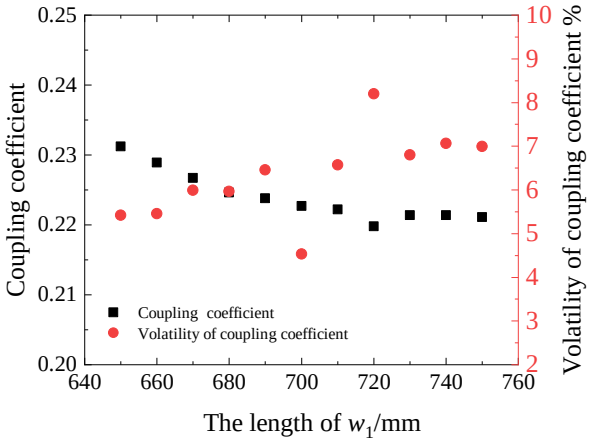

FIGURE 10. Simulation plots of ISC structure coupling coefficients and fluctuation rate of coupling coefficients after a 200 mm offset for various ferrite sizes.

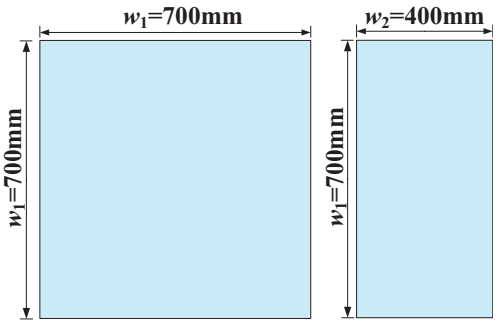

FIGURE 11. Dimensional drawings of ferrite.

4. MAXWELL THEORY SIMULATION VERIFICATION AND EFFECT DEMONSTRATION

After deriving the optimal parameters of the ISC structure and the ferrite parameters, this section conducts a 2 kW simulation experiment by constructing a Maxwell simulation model of the ISC structure, as illustrated in Fig. 12. This is carried out to verify the superiority and accuracy of the optimization results.

Finally, the simulation results of the coupling coefficients of the ISC structure without ferrite and the ISC structure with ferrite are obtained as shown in Fig. 13. From the figure, it can be seen that the coupling coefficients of the ISC structure exhibit an increasing and then decreasing trend with the increase of the offset distance, regardless of whether ferrite is added or not. Among them, the maximum fluctuation rate of the coupling coefficient for the ISC structure without ferrite is 3.5%, while the maximum fluctuation rate of the coupling coefficient for the ISC structure with ferrite is 4.5%. Additionally, after incorporating the ferrite structure designed in this study, the coupling coefficient enhancement rate of the ISC coil can exceed 110%.

Meanwhile, as shown in Fig. 14, the magnetic simulation experiment of the Maxwell coil revealed that the magnetic field size of the ferrite-free ISC structure, located 800 mm on both sides of the driving direction of the electric vehicle, is 5.354 μT at the power level of 2 kW. However, the magnetic field size can be reduced to 0.911 μT after adding the magnetic core, resulting in an electromagnetic shielding effect as high as 82.98%.

5. MAXWELL THEORY SIMULATION VERIFICATION AND EFFECT DEMONSTRATION

After the aforementioned design, optimization, screening, and simulation verification, the ISC structure is experimentally verified in this section. This also validates the accuracy and superiority of the ISC structure with ferrite and the parameters proposed in this paper.

5.1. Brief Analysis of the Experimental Procedure

Firstly, a complete set of 2 kW dynamic wireless energy transmission system device as shown in Fig. 15(a), as well as the transmitting coil in Fig. 15(b) and the receiving coil in Fig. 15(c), was built according to the optimization results in

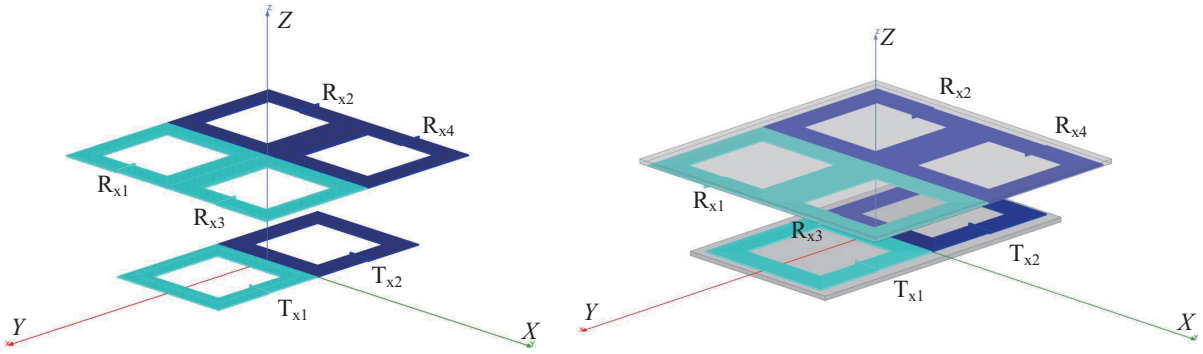

FIGURE 12. Simulation of ISC structure.

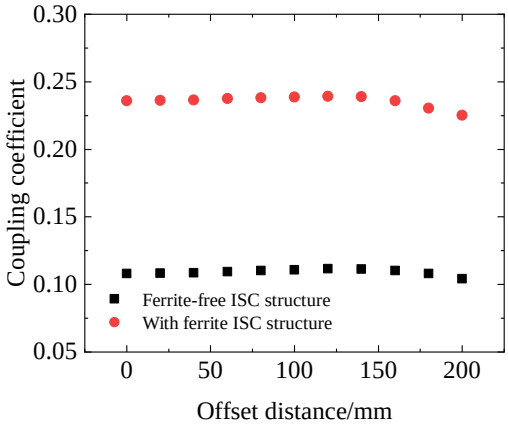

FIGURE 13. Simulated values of coupling coefficients for ISC structure.

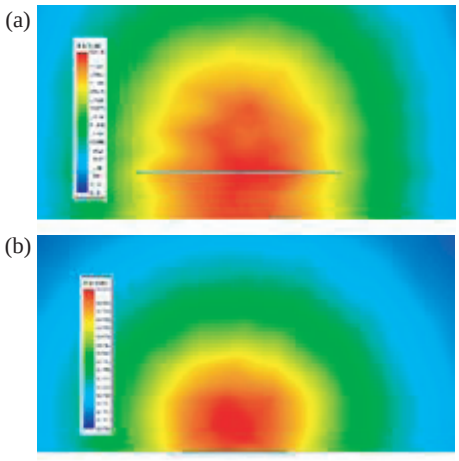

FIGURE 14. Simulated values of leakage magnitude at 800 mm for ISC structure. (a) Ferrite-free. (b) With ferrite.

Table 1. As can be seen from the figure, the main components of the complete setup are a DC power supply, an RT-unit inverter-rectifier module, an S-S topology, a transmitting coil, a receiving coil, an oscilloscope, an NF-5035S electromagnetic radiation analyzer, and a variable load. During the experiment, all the Leeds wires used were of size $\varphi 0.1\,\text{mm} \times 800$ strands, with a wire diameter of $r = 3.9\,\text{mm}$ and a maximum withstand current of 31.415 A. Additionally, the air gap between the coils was set to be $d = 150\,\text{mm}$. Finally, detailed information on the other parameters of the system involved in the experiment is shown in Table 2.

TABLE 2. Measured parameters of the system during the experiment.

Parameter	Physical meaning	Value
$L_1/\mu\text{H}$	Self-inductance of the transmitting coil	501.79
$L_2/\mu\text{H}$	Self-inductance of the receiving coil	891.97
C_1/nF	Compensation capacitance of transmitter coil	7.36
C_2/nF	Compensation capacitance of receiving coil	4.25
$R_1/\text{m}\Omega$	Resistance of the transmitting coil	800
$R_2/\text{m}\Omega$	Resistance of the receiving coil	1010
f_0/kHz	Working frequency	85
R/Ω	Load Equivalent Resistance	30

The experimental procedure is as follows: firstly, using the IM3536 impedance analyzer, the self-inductance, mutual inductance, and internal resistance of the ISC structure are measured. The experimental values of the coupling coefficients k_e and fluctuations ε_X of the ISC structure are then calculated by combining Eq. (11) and Eq. (18). Subsequently, the resonant state is determined by analyzing the voltage-current waveforms between the transmitter coil and receiver coil displayed on the oscilloscope. When the resonance state is achieved, the system transmission efficiency is calculated by adjusting the voltage of the DC power supply using the WT5000 power analyzer. The magnetic field changes at the target surface are detected by the NF-5035S electromagnetic radiation analyzer and its accompanying MCS electromagnetic radiation analysis software. Finally, the experimental results are compared and analyzed with the simulation ones to validate the superiority and accuracy of the ISC coil structure and each parameter proposed in this paper.

5.2. Verification of Anti-Offset Performance

In terms of the anti-offset performance in the horizontal X-direction, the offset is adjusted in increments of 20 mm, with a limit of $\pm 200\,\text{mm}$. The measured results of the ISC coil coupling coefficients in the X-positive direction are shown in Table 3. By combining the data from Table 3 with the simulation

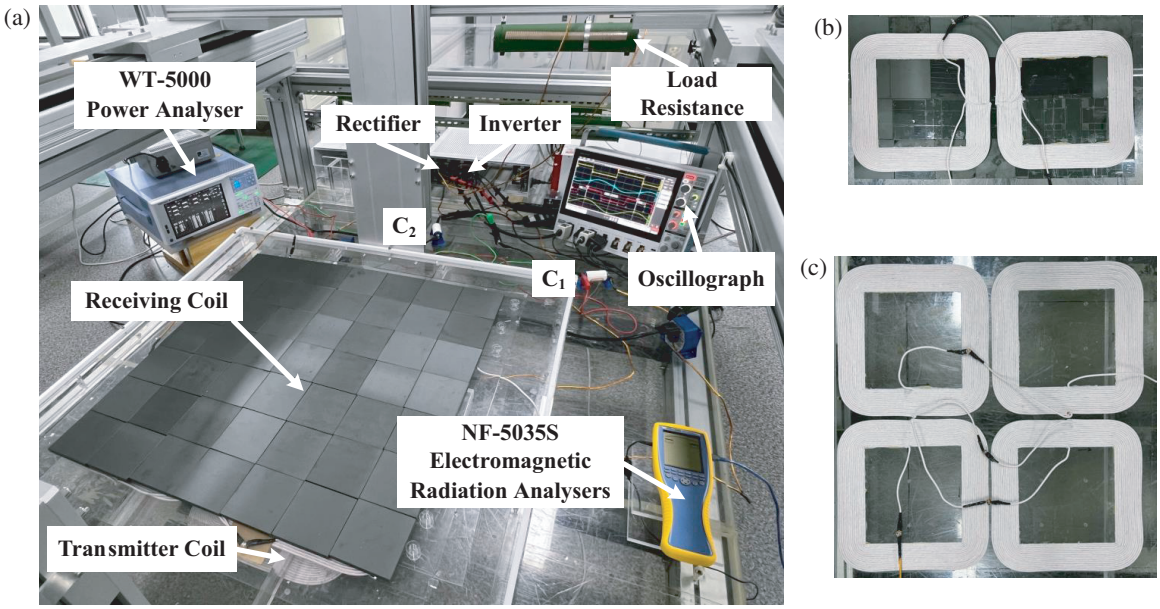

FIGURE 15. A complete diagram of a dynamic wireless energy transmission system.

TABLE 3. Measured values of coupling coefficient for ISC structure.

Offset distance/mm	Coupling coefficient	Volatility %
0	0.2271	/
20	0.2272	0.04
40	0.2276	0.22
60	0.2287	0.70
80	0.229	0.84
100	0.2298	1.19
120	0.2302	1.37
140	0.2299	1.23
160	0.2271	0
180	0.2217	2.38
200	0.2168	4.54

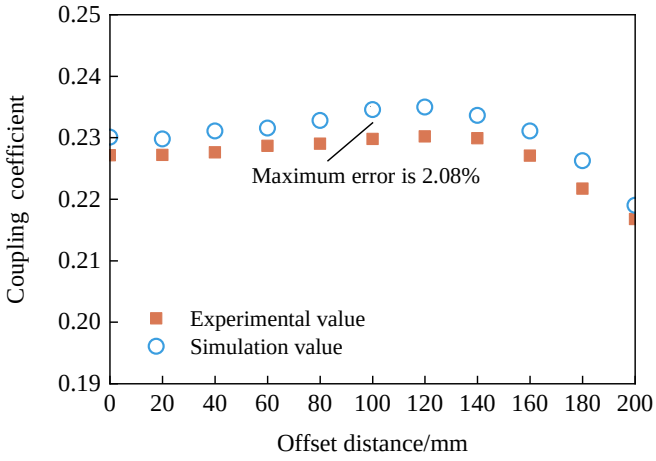

FIGURE 16. Coupling coefficients of the ISC structure after offset in the X-direction.

results depicted in Fig. 13, the coupling coefficient simulation and experimental comparison graphs are illustrated in Fig. 16. The comparison reveals that the measured and simulated values of the coupling coefficients exhibit a maximum error of 2.08% at an offset of 100 mm, a minimum error of 1.05% at an offset of 200 mm, and an average error of 1.59%. Furthermore, the graph demonstrates that the coupling coefficient variation of the ISC structure proposed in this study displays a saddle shape, unlike the traditional rectangular coil coupling coefficient, which shows a monotonically decreasing trend. The coupling coefficient of the ISC structure starts at $k = 0.2271$ in the orthogonal state, gradually increases with the offset distance, peaks at $k = 0.2302$ at 120 mm, and then gradually decreases until it reaches the minimum at $k = 0.2168$ at 200 mm. By utilizing Eq. (18), the maximum fluctuation rate of the experimental value of the coupling coefficient $\varepsilon_{X\max} = 4.54\%$ can be calculated.

Similarly, since the ISC structure is a symmetric structure, the variation of the coupling coefficients in the X-negative direction should be similar to that in the positive direction. Overall, the experimental and simulated values of the ISC structure are essentially identical, which validates the X-direction offset resistance of the ISC coil structure.

5.3. Verification of Magnetic Shielding Effect

The magnitude of the leakage magnetic field B_p of the ISC coil without ferrite and the ISC structure with ferrite is measured by the NF-5035S electromagnetic radiation analyzer under a 2 kW experimental condition. The measurements are taken at 800 mm on both sides of the driving direction of the electric vehicle, with an X-direction offset ranging from 0 to 200 mm. The results are shown in Fig. 17. From the figure, it can be seen that the maximum error between the measured and simulated

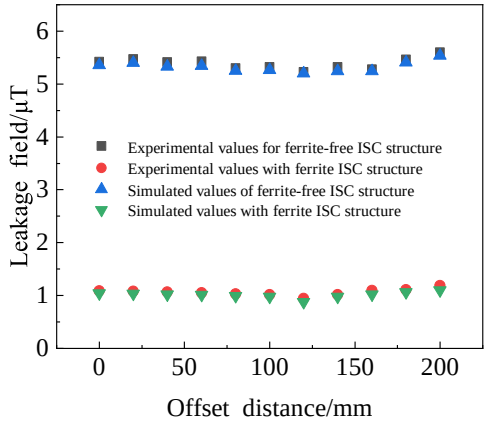

FIGURE 17. Comparison of measured and simulated leakage magnetic fields at 800 mm on either side of the direction of motion for ISC structure with and without ferrite.

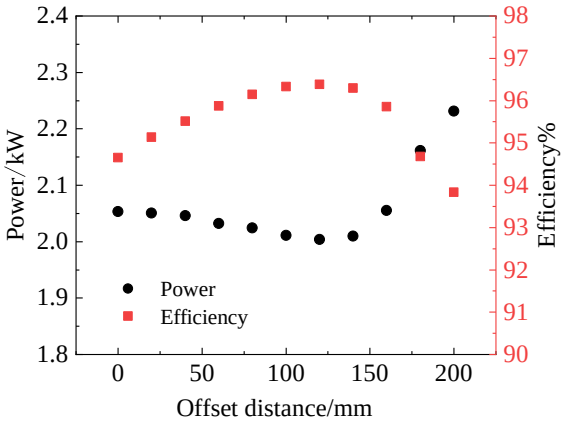

FIGURE 18. Efficiency and output power of the ISC structure after offsetting along the X-direction.

values of the leakage magnetic field of the ISC structure without ferrite is only 1.61%, while the maximum error between the measured and simulated values of the leakage magnetic field of the ISC structure with ferrite is 3.26%. The error between the magnetic field simulation value B_c and magnetic field measurement value B_p is defined as ε_{cp}, and the expression is as follows:

$$\varepsilon_{\mathrm{cp}} = \left| \frac{B_{\mathrm{c}} - B_{\mathrm{p}}}{B_{\mathrm{p}}} \right| \times 100\% \tag{20}$$

In addition, the leakage magnetic field located at 800 mm decreases by 79.89% from 5.42 μT to 1.09 μT for the case where the transmitting and receiving coils are directly opposite each other after the addition of ferrite. Meanwhile, the leakage magnetic field located at 800 mm decreases by 78.93% from 5.6 μT to 1.18 μT after the offset of 200 mm. The reduction between the measured value B_{cn} of the leakage magnetic field of the ISC coil without ferrite located at 800 mm and the measured value B_{ch} of the leakage magnetic field of the ISC coil with ferrite located at 800 mm is defined as ε_{cnh}, and the expression is as follows:

$$\varepsilon_{\mathrm{cnh}} = \frac{B_{\mathrm{cn}} - B_{\mathrm{ch}}}{B_{\mathrm{cn}}} \times 100\% \tag{21}$$

5.4. Power and Efficiency

To verify the superiority of the ISC structure, its output power and efficiency are measured in this section. Using a WT-5000 power analyzer, the coupling efficiency between the transmitting and receiving coils is determined. Fig. 18 illustrates the transmission efficiency and output power of the ISC coil structure at various offset distances along the X-positive direction. It is observed that the transmission efficiency value increases and then decreases with the offset distance increment, which aligns with the coupling coefficient trend in Fig. 10. The maximum efficiency is 96.37% when the coil is offset by 120 mm, and the minimum efficiency is 93.83% when the coil is offset by 200 mm. The offset ranges from 0 mm to 200 mm, with the maximum output power at 2.23 kW and the minimum at 2 kW. The maximum fluctuations in efficiency and power are 2.64% and 11.33%, respectively.

Similarly, the ISC structure is a symmetrical structure, so the variation of efficiency and power in the X-negative direction should be similar to that in the positive direction. The results show that the fluctuation rate of the transmission efficiency during the offset process is very small. This is attributed to the fact that the coupling coefficient of the system remains almost constant for different degrees of offset along the X direction in the ISC coil structure.

5.5. Comparison Group Experiment

In order to further confirm and verify the advantages of the new structure, this paper compares the ISC structure with two other different groups of coil structures.

As shown in Fig. 19, the comparison group 1 is a conventional rectangular coil with various parameters as shown in Table 4, which is labeled as R_T in this paper. Fig. 20 shows comparison group 2, whose parameters are shown in Table 4 and labeled as R_D in this paper.

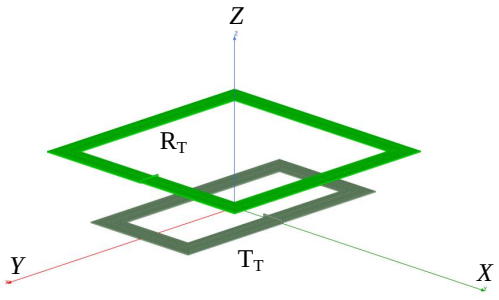

FIGURE 19. Structural simulation of R_T coil.

From Fig. 21, it can be seen that the coupling coefficient of the R_T coil in the X-direction shows a monotonically decreasing trend with the increase of the offset distance. From the offset of 0 mm to 200 mm, the coupling coefficient decreases from 0.188 to 0.151, and the maximum value of the fluctuation rate of the coupling coefficient in this process reaches 19.68%. The coupling coefficient of the R_D coil in the X-direction also

TABLE 4. Experimental parameters of the R_T and R_D coils.

Coils	Inner length/mm	Inner width/mm	Outer length/mm	Outer width/mm	Turns
T_T	547	220	672	346	16
R_T	550	550	670	670	15
T_{D1}	220	220	340	340	15
T_{D2}	220	220	340	340	15
R_{D1}	547	220	672	346	16
R_{D2}	547	220	672	346	16

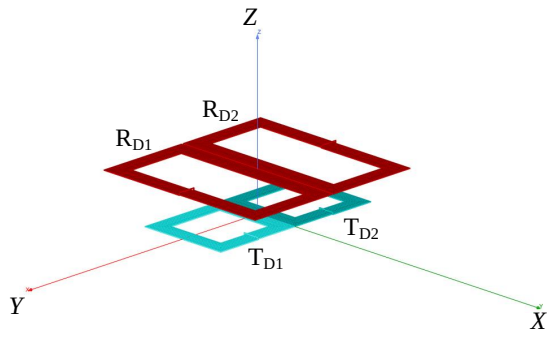

FIGURE 20. Structural simulation of the R_D coil.

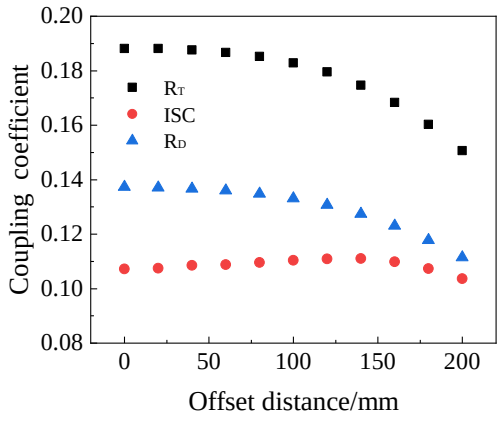

FIGURE 21. Plot of variation of coupling coefficients during coil offset for ISC structure and comparison group.

shows a monotonically decreasing trend with the increase of the offset distance. From the offset of 0 mm to 200 mm, the coupling coefficient decreases from 0.1345 to 0.1091, and the maximum value of the fluctuation rate of the coupling coefficient reaches 18.88%. The coupling coefficient of the ferrite-free ISC structure shows a saddle-like shape in the X-direction with the increase of the offset distance, which is initially increasing and then decreasing. The coupling coefficient increases from 0.1072 in the orthogonal state to the maximum value of 0.111 at the offset of 140 mm, and then decreases to the minimum value of 0.1037 at the offset of 200 mm. During this period, the maximum fluctuation rate of the coupling coefficient reaches 3.54%.

The maximum coupling coefficient fluctuation of the two comparison groups of coils mentioned above during offset is significantly greater than the 3.54% of the ISC structure proposed in this paper.

Figure 22 illustrates the output power variation of the three coil structures during the offsetting process. The figure shows that when the R_T coil is offset from the orthogonal state to 200 mm, the transmitted power changes from 2.052 kW to 3.139 kW, with a maximum fluctuation rate of 52.97% in its output power. Similarly, when the R_D coil is offset to 200 mm from the forward state, the transmitted power changes from 2.034 kW to 3.026 kW, with a maximum fluctuation rate of 48.12% in its output power. In contrast, when the ferrite-free ISC structure is offset to 200 mm from the orthogonal state, the transmitted power initially decreases from 2.076 kW to 1.99 kW and then increases to 2.219 kW, with a maximum fluctuation rate of 6.89% in its output power.

The fluctuation rate of the maximum output power of the two comparison group coils mentioned above is significantly higher than the 6.89% fluctuation rate for the ISC structure.

Figure 23 illustrates the transmission efficiency of the three coil structures at different offset distances. It can be observed that the R_T and R_D coil structures show a monotonically decreasing trend in transmission efficiency, while the ISC coil structure displays a saddle shape. When the R_T coil is offset from the forward state to 200 mm, the transfer efficiency ranges from 90.48% to 78.92%, with a maximum fluctuation of 12.78% in the transfer efficiency. The R_D coil ranges from 94.54% to 85.61%, with a maximum fluctuation of 9.45% when being offset from the forward state to 200 mm. The ferrite-free ISC coil increases from 93.99% to 95.7% and then decreases to 93.17%, with a maximum fluctuation of 1.82% in the transmission efficiency when being offset from the forward state to 200 mm.

Upon comparison, it can be found that the maximum fluctuation in efficiency of the two coils mentioned above during offset exceeds 1.82% of the ISC structure proposed in this paper.

Figure 24 illustrates the magnetic field strength trend at 800 mm on both sides of the motion direction during the offset process for the three coil configurations at a power of 2 kW. The figure indicates that when the offset distance is consistent, the leakage magnetism of both the R_T coil and R_D coil is greater than that of the ISC coil. Consequently, the ISC coil has a better ability to shield the magnetic field.

Due to the limitations of laboratory equipment, the ISC structure designed in this paper aims to provide some reference significance for anti-deviation and magnetic shielding in the field

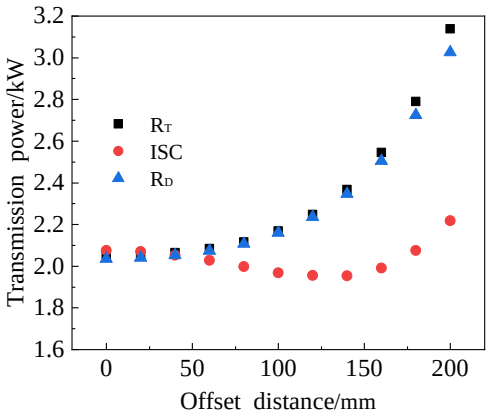

FIGURE 22. Transmitted power of the ISC structure and comparison group coils during the offsetting process.

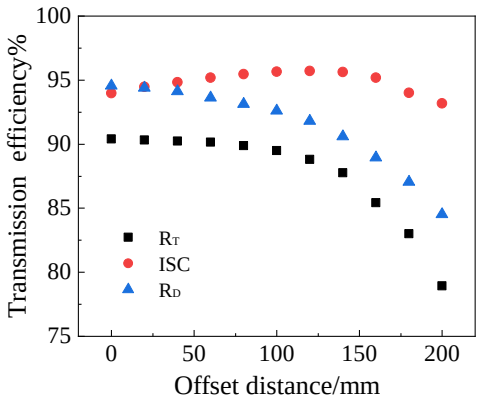

FIGURE 23. Transmission efficiency of ISC structure compared to group coils during offsets.

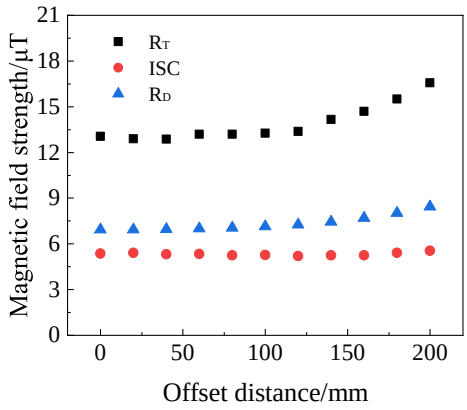

FIGURE 24. Variation of magnetic field strength at 800 mm on both sides of the motion direction during deflection of the ISC structure with the comparison group coil at 2 kW power.

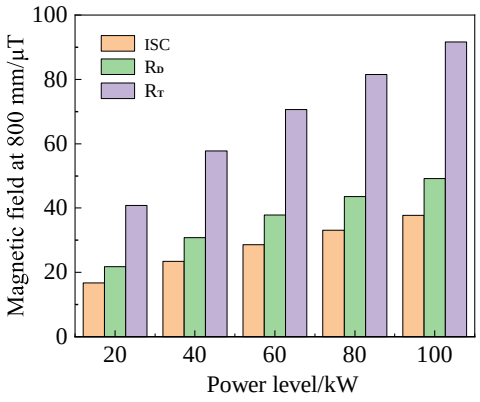

FIGURE 25. Magnetic field strength of the ISC structure at high power was compared to the group of coils located 800 mm on either side of the direction of motion during the offset process.

TABLE 5. Comparison of experimental parameter performance in literature.

References	Size of Tx ($L \times W$/mm)	Size of Rx ($L \times W$/mm)	Maximum offset distance	Coupling coefficient volatility%	Maximum power fluctuation rate%	Maximum efficiency volatility%	Magnetic shielding capability
[21]	350∗358	660∗620	175	3.12	7.93	2.79	/
[22]	300∗200	1000∗800	300	/	50	30.1	/
[23]	390∗390	390∗390	150	/	/	7.8	/
our work	340∗340	680∗680	200	4.54	11.33	2.64	✓

'/' denotes that the value is not given in the references. (Length × width) is abbreviated as ($L \times W$)

of rail transport. Therefore, only experiments with a power of 2 kW and comparative tests were conducted. To closely mimic real-life conditions and better verify the magnetic shielding effect of the proposed structure, high-power simulation experiments were carried out in this section, and the experimental results are depicted in Fig. 25. Since the power level has minimal impact on the anti-offset effect, this section focuses solely on studying the magnetic shielding effect. From the figure, it is evident that as the power level increases from 20 kW to 100 kW, the ISC structure outperforms the R_D coil and R_T coil in terms of magnetic shielding effectiveness.

Table 5 compares the performance of the ISC structure proposed in this paper with other references. Compared with [22–24], the ISC structure proposed in this paper also possesses better magnetic shielding capability without requiring any auxiliary equipment at lower coupling coefficients, transmission efficiencies, and output power variability.

6. CONCLUSION

The paper proposes an integrated symmetrical coil structure and introduces an optimization algorithm to optimize its parameters. Following this, the ferrite parameters are optimized using Maxwell software based on the optimal coil structure parameters. Compared to existing coil structures, the ISC structure offers strong resistance to deflection in the X-direction and reduces magnetic field leakage from the Autonomous Rail Rapid Transit at 800 mm on the side of the doors. Experimental results show that the ISC structure with ferrite addition achieves a high coupling coefficient of 0.2392 with a fluctuation rate less than 5%, and the system's highest transmission efficiency reaches 96.37% at an offset of ± 200 mm in the X-direction. This experimental validation confirms the effectiveness of the ISC structure in resisting deflection and addressing magnetic leakage issues in high-power scenarios. Overall, the ISC structure is highly suitable for urban rail transport applications.

ACKNOWLEDGEMENT

This work was supported in part by the Natural Science Foundation of Hunan Province under Grants 2022JJ30226, National Key R&D Program Project (2022YFB3403200) and Natural Science Foundation of Hunan Province (2023JJ50202).

REFERENCES

[1] Kim, J., J. Kim, S. Kong, H. Kim, I.-S. Suh, N. P. Suh, D.-H. Cho, J. Kim, and S. Ahn, "Coil design and shielding methods for a magnetic resonant wireless power transfer system," *Proceedings of the IEEE*, Vol. 101, No. 6, 1332–1342, 2013.

[2] Zhao, J. Y., J. X. Zhao, Y. L. Cui, and et al., "Research on transmission characteristics of MC R-WPT system with asymmetrical compensation," *Journal of Electronic Measurement and Instrumentation*, Vol. 32, No. 2, 106–112, 2018.

[3] Cheng, J., X. Wu, and Z. Bai, "Maximum efficiency tracking of wireless power transfer for electric vehicles based on coupling coefficient estimation," *Journal of Electronic Measurement and Instrumentation*, Vol. 34, No. 3, 180–186, 2020.

[4] Ahn, J., J. Kim, D. Park, H. Kim, and S. Ahn, "An active shielding control method for a wireless power transfer system under misalignment conditions," *Journal of Electromagnetic Engineering and Science*, Vol. 22, No. 1, 56–63, 2022.

[5] Shen, D., G. Du, D. Qiu, and B. Zhang, "Research status and development trend of electromagnetic compatibility of wireless power transfer system," *Transactions of China Electrotechnical Society*, Vol. 35, 2855–2869, 2020.

[6] Xue, M., Q. Yang, P. Zhang, J. Guo, Y. Li, and X. Zhang, "Application status and key issues of wireless power transmission technology," *Transactions of China Electrotechnical Society*, Vol. 36, No. 8, 1547–1568, 2021.

[7] Kim, S., H.-H. Park, J. Kim, J. Kim, and S. Ahn, "Design and analysis of a resonant reactive shield for a wireless power electric vehicle," *IEEE Transactions on Microwave Theory and Techniques*, Vol. 62, No. 4, 1057–1066, 2014.

[8] Lee, S., D.-H. Kim, Y. Cho, H. Kim, C. Song, S. Jeong, J. Song, G. Park, S. Hong, J. Park, and et al., "Low leakage electromagnetic field level and high efficiency using a novel hybrid loop-array design for wireless high power transfer system," *IEEE Transactions on Industrial Electronics*, Vol. 66, No. 6, 4356–4367, 2019.

[9] Chen, C., X. Huang, L. Tan, and et al., "Electromagnetic environment and security evaluation for wireless charging of electric vehicles," *Transactions of China Electrotechnical Society*, Vol. 30, No. 19, 61–67, 2015.

[10] Dong, L., F. H. Lin, C. H. Wang, *et al.*, "Assessing human exposure to electromagnetic fields from catenary-freepower supply urban rail transit vehicle," *Transactions of China Electrotechnical Society*, Vol. 36, No. S1, 40–45, 2021.

[11] Zhu, Q., D. Chen, L. Wang, C. Liao, and Y. Guo, "Study on the magnetic field and shielding technique for an electric vehicle oriented wireless charging system," *Transactions of China Electrotechnical Society*, Vol. 30, No. S1, 143–147, 2015.

[12] Covic, G. A. and J. T. Boys, "Modern trends in inductive power transfer for transportation applications," *IEEE Journal of Emerging and Selected Topics in Power Electronics*, Vol. 1, No. 1, 28–41, 2013.

[13] Li, Z., X. Xiong, L. Ren, P. Kong, Y. Zhang, and J. Li, "Design and optimization of quasi-constant coupling coefficients for superimposed dislocation coil structures for dynamic wireless charging of electric vehicles," *Progress In Electromagnetics Research M*, Vol. 116, 23–38, 2023.

[14] Xu, Q., Y. Xu, and R. Mai, "IPT resonant reactive shielding systems with the characteristics of optimal magnetic shielding effect on the target surface," *Proceedings of the CSEE*, Vol. 39, No. 18, 5490–5498+5597, 2019.

[15] Park, J., D. Kim, K. Hwang, *et al.*, "A resonant reactive shielding for planar wireless power transfer system in smartphone application," *IEEE Transactions on Electromagnetic Compatibility*, Vol. 59, No. 2, 695–703, 2017.

[16] Cruciani, S., T. Campi, F. Maradei, and M. Feliziani, "Active shielding design for a dynamic wireless power transfer system," in *2020 International Symposium on Electromagnetic Compatibility — EMC EUROPE*, 1–4, Rome, Italy, 2020.

[17] Li, Z., Z. Gan, L. Ren, P. Kong, X. Xiong, Y. Cheng, and X. Zhou, "Omni-directional wrap-around active magnetic shield structure with high efficiency and low magnetic leakage for wireless power transfer systems," *Journal of Electronic Measurement and Instrumentation*, Vol. 38, No. 1, 94–105, 2024.

[18] Li, Z., S. Li, J. Li, Y. Zou, and S. Huang, "Mutual inductance calculation and optimization of multiple receiving coils in positive and negative series structure for dynamic wireless energy transmission system," *Journal of Electrotechnology*, Vol. 36, 5153–5164, 2021.

[19] Dou, R. T., *et al.*, "Review on the application development and research of electromagnetic shielding of magnetically coupled resonant wireless power transfer system," *Proceedings of the CSEE*, Vol. 43, 6020–6040, 2023.

[20] Li, J. Y., *et al.*, "Research progress on electromagnetic interference suppression of magnetically coupled wireless power transfer system," *Proceedings of the CSEE*, Vol. 42, 7387–7403, 2022.

[21] Mi, M., Q. Yang, Y. Li, P. Zhang, and W. Zhang, "Multi-objective active shielding coil design for wireless electric vehicle charging system," *IEEE Transactions on Magnetics*, Vol. 58, No. 2, 8700505, 2022.

[22] Li, Z., X. Xiong, L. Ren, P. Kong, Y. Zhang, and J. Li, "Design and optimization of quasi-constant coupling coefficients for superimposed dislocation coil structures for dynamic wireless charging of electric vehicles," *Progress In Electromagnetics Research M*, Vol. 116, 23–38, 2023.

[23] Choi, S. Y., S. Y. Jeong, B. W. Gu, G. C. Lim, and C. T. Rim, "Ultraslim S-type power supply rails for roadway-powered electric vehicles," *IEEE Transactions on Power Electronics*, Vol. 30,

No. 11, 6456–6468, 2015.

[24] Xiao, H., Q. Zhou, S. Xiong, *et al.*, "Wireless power transfer system based on double-layer quadrature double-D coupling structure with anti-misalignment and anti-deflection," *Transactions of China Electrotechnical Society*, Vol. 37, No. 16, 4004–4018, 2022.